Mapping Phosphorylated Tau using Multidimensional MRI in Alzheimer's Disease

Hongyi Zhang[1], Caitlin S. Latimer[2], C. Dirk Keene[2], Dan Benjamini[3], Shinjini Kundu[1]

[1]Washington University in St. Louis, St. Louis, MO, USA

[2]University of Washington, Seattle, WA, USA

[3]National Institutes of Health, Bethesda, MD, USA

October 29, 2025

1 Abstract (746/750 words)

INTRODUCTION: Alzheimer's disease (AD) is a progressive neurodegenerative disorder that severely impairs memory and cognition, posing an increasing public health challenge worldwide. Current research suggests that AD is strongly linked to the abnormal accumulation of phosphorylated tau (pTau), a pathological hallmark reflecting neuronal dysfunction and neurodegeneration[1]. Clinically, pTau is typically assessed via cerebrospinal fluid (CSF) analysis or tau positron emission tomography (tau-PET)[2]. Although informative, CSF analysis is invasive, and tau-PET requires ionizing radiation. Furthermore, tau-PET is limited in routine clinical settings due to its high cost and radiation exposure. There remains an urgent need for a non-invasive, safe, and widely applicable imaging method to characterize the spatial distribution and concentration of pTau in the human brain to support a biologically based diagnosis of AD.

METHODS: To address this need, this research proposes an imaging framework that integrates multidimensional MRI (MD-MRI)[3] with supervised machine learning to estimate voxelwise pTau concentration and its spatial distribution. The approach leverages the rich microstructural information embedded in the voxelwise diffusion-relaxation probability distributions derived from MD-MRI[4,5]. Eight postmortem human brain slices from four donors were analyzed. Voxelwise 2D joint distributions of T1, T2, and Mean Diffusivity (T1D and T2D) were derived from MD-MRI, and vectorized joint distributions were applied as input features. Histology-derived pTau concentrations and spatial distributions from the same samples, quantified via immunohistochemistry, served as the ground truth. pTau concentration was stratified into either 2 classes (high vs. low) or 3 classes (low, moderate, high) for subsequent classification. To comprehensively evaluate the framework's effectiveness, multiple regression and classification models were employed to predict pTau concentration. Before model training, to eliminate the influence of imaging artifacts, only valid voxels within the region of interest were retained according to the binary mask. To simplify the data structure and improve computational efficiency, principal component analysis (PCA) with 95% threshold was applied for dimensionality reduction. During the training phase, a nested cross-validation (5 outer folds and 5 inner folds) was employed to assess model generalizability, while Bayesian optimization was used to select the optimal hyperparameters within each inner loop. For regression tasks, we compared linear regression, quadratic regression, support vector regression (SVR), random forest, and multilayer perceptron (MLP). For 2-class and 3-class classification tasks, we evaluated logistic regression, Fisher's linear discriminant (FLD), support vector machine (SVM), random forest (RF), and multilayer perceptron (MLP).

RESULTS: The results demonstrated that the random forest model consistently achieved the best and most stable performance across all tasks. For regression, random forest achieved the lowest mean squared errors and highest goodness of fit for both T1D (MSE 0.031 ± 0.001, $R^2 = 0.797 \pm 0.007$) and T2D (MSE 0.040 ± 0.001, $R^2 = 0.724 \pm 0.005$). For 2-class classification, this model reached accuracies and Cohen's kappa, respectively, of 0.924 ± 0.002 and 0.803 ± 0.001 for T1D, and 0.909 ± 0.003 and 0.779 ± 0.009 for T2D. For 3-class classification, the model achieved accuracies of 0.879 ± 0.004 for T1D and 0.858 ± 0.005 for T2D, with corresponding Cohen's kappa values of 0.841 ± 0.004 for T1D and 0.820 ± 0.006 for T2D, respectively. These findings underscore the robustness of the random forest model. It consistently demonstrated superior

predictive capability across both regression and classification tasks. Importantly, the reconstructed imaging maps based on the coordinates of each voxel visually demonstrate a strong concordance between the model predictions and the histology-derived pTau distributions and concentrations, confirming the validity of the approach. Quantitatively, this agreement was confirmed by the structural similarity index measure (SSIM) analysis, with mean SSIM values of 0.82 and 0.81 for regression, 0.90 and 0.89 for binary classification, and 0.87 and 0.86 for 3-class classification on the T1D and T2D data, respectively.

DISCUSSION: These results demonstrate that the T1D and T2D diffusion–relaxation joint distributions of MD-MRI encode rich microstructural information related to tau pathology, and the random forest model can effectively capture this information to predict pTau concentration. The strong spatial correspondence and high SSIM values confirm that the reconstructed images reflect clinically meaningful and biologically relevant patterns of pTau accumulation.

CONCLUSION: Overall, this study establishes a proof of concept that MD-MRI–derived joint distributions can non-invasively capture tau pathology in Alzheimer's disease. This framework may potentially provide a safe and non-invasive alternative to CSF analysis and tau-PET in clinical diagnosis. In the future, this approach may have potential clinical utility as a marker of tau pathology. Future work will extend this framework to in vivo human datasets to validate its clinical applicability.

2 Keywords (5/5 keywords)

Multidimensional MRI; Alzheimer's Disease; Phosphorylated Tau; Machine Learning; Random Forest.

3 Synopsis (94/100 words)

Motivation: Phosphorylated tau accumulation drives neurodegeneration and cognitive decline in Alzheimer's disease, yet current clinical assays rely on invasive CSF assays or ionizing tau-PET imaging, underscoring the need for a safe and non-invasive alternative.

Goal: This study develops an MD-MRI framework integrating supervised machine learning to estimate voxelwise distributions and concentrations of pTau.

Approach: Ex vivo datasets were processed with PCA and nested cross-validation across multiple regression and classification models.

Results: Random Forest achieved the highest and most stable performance, and reconstructed MD-MRI pTau maps showed strong concordance with histology, confirming the framework's effectiveness for non-invasive tau mapping.

4 Impact (38/40 words)

This study introduces a novel framework integrating multidimensional MRI with supervised learning to safely and non-invasively map phosphorylated tau, providing a transformative imaging biomarker that may redefine how Alzheimer's disease progression is monitored in research and clinical practice.

5 References

1. Wang Y, Mandelkow E. Tau in physiology and pathology. Nat Rev Neurosci. 2016 Jan;17(1):5-21. doi: 10.1038/nrn.2015.1. PMID: 26631930.

2. Jack CR Jr, Bennett DA, Blennow K, et al. NIA-AA Research Framework: Toward a biological definition of Alzheimer's disease. Alzheimers Dement. 2018 Apr;14(4):535-562. doi: 10.1016/j.jalz.2018.02.018. PMID: 29653606.

3. Benjamini D, Bouhrara M, Komlosh ME, et al. Multidimensional MRI for Characterization of Subtle Axonal Injury Accelerated Using an Adaptive Nonlocal Multispectral Filter. Front Phys. 2021;9:737374. doi: 10.3389/fphy.2021.737374. PMID: 37408700.
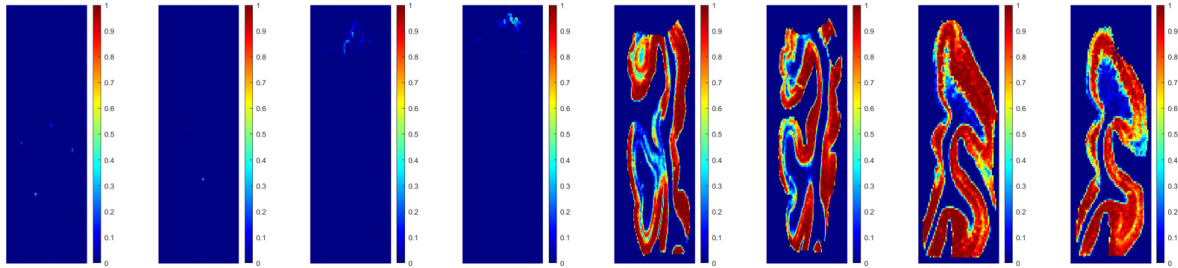
4. Kundu S, Barsoum S, Ariza J, et al. Mapping the individual human cortex using multidimensional MRI and unsupervised learning. Brain Commun. 2023;5(6):fcad258. doi: 10.1093/braincomms/fcad258. PMID: 37953850.

5. Barsoum S, Latimer CS, Nolan AL, et al. Multidimensional MRI reveals cortical astrogliosis linked to dementia in Alzheimer's disease. Brain Commun. 2025;7(3):fcaf245. doi: 10.1093/braincomms/fcaf245. PMID: 40585810.

6 Tables and Figures (5/5 Figures, 500 characters per caption)
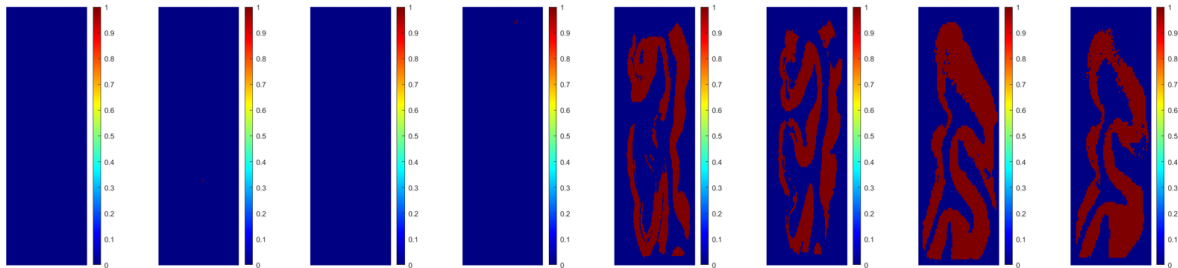
Table 1: Performance comparison across all models and tasks (Nested Cross-Validation)

| **Regression Models**	**T1D**		**T2D**	
Model	MSE	R^2	MSE	R^2
Linear Regression	0.097 ± 0.001	0.335 ± 0.006	0.104 ± 0.001	0.289 ± 0.006
Quadratic Regression	0.094 ± 0.001	0.356 ± 0.004	0.100 ± 0.001	0.318 ± 0.007
SVR (Linear)	0.107 ± 0.006	0.269 ± 0.044	0.116 ± 0.006	0.203 ± 0.043
SVR (RBF)	0.055 ± 0.011	0.624 ± 0.073	0.083 ± 0.040	0.430 ± 0.273
Random Forest Regression	0.031 ± 0.001	0.797 ± 0.007	0.040 ± 0.001	0.724 ± 0.005
MLP Regression	0.035 ± 0.003	0.762 ± 0.019	0.042 ± 0.003	0.714 ± 0.018
2-class Classification Models	**T1D**		**T2D**	
Model	Accuracy	Kappa	Accuracy	Kappa
Logistic Regression	0.811 ± 0.003	0.491 ± 0.010	0.775 ± 0.003	0.370 ± 0.006
FLD	0.805 ± 0.002	0.475 ± 0.006	0.776 ± 0.002	0.377 ± 0.004
SVM (Linear)	0.812 ± 0.004	0.486 ± 0.012	0.770 ± 0.003	0.326 ± 0.006
SVM (RBF)	0.921 ± 0.004	0.801 ± 0.001	0.901 ± 0.004	0.774 ± 0.010
Random Forest Classification	0.924 ± 0.002	0.803 ± 0.001	0.909 ± 0.003	0.779 ± 0.009
MLP Classification	0.919 ± 0.002	0.797 ± 0.004	0.868 ± 0.079	0.606 ± 0.339
3-class Classification Models	**T1D**		**T2D**	
Model	Accuracy	Kappa	Accuracy	Kappa
Logistic Regression	0.767 ± 0.002	0.720 ± 0.002	0.730 ± 0.002	0.685 ± 0.002
FLD	0.756 ± 0.004	0.705 ± 0.003	0.730 ± 0.002	0.681 ± 0.001
SVM (Linear)	0.769 ± 0.001	0.725 ± 0.001	0.728 ± 0.002	0.689 ± 0.002
SVM (RBF)	0.876 ± 0.006	0.839 ± 0.005	0.857 ± 0.013	0.818 ± 0.012
Random Forest Classification	0.879 ± 0.004	0.841 ± 0.004	0.858 ± 0.005	0.820 ± 0.006
MLP Classification	0.874 ± 0.004	0.837 ± 0.005	0.854 ± 0.006	0.814 ± 0.006
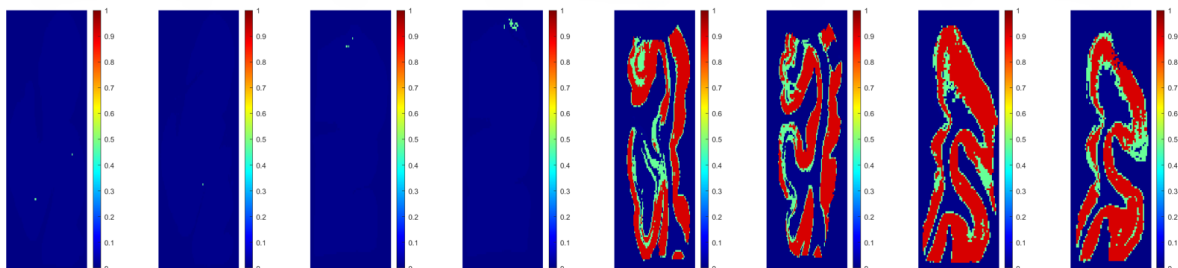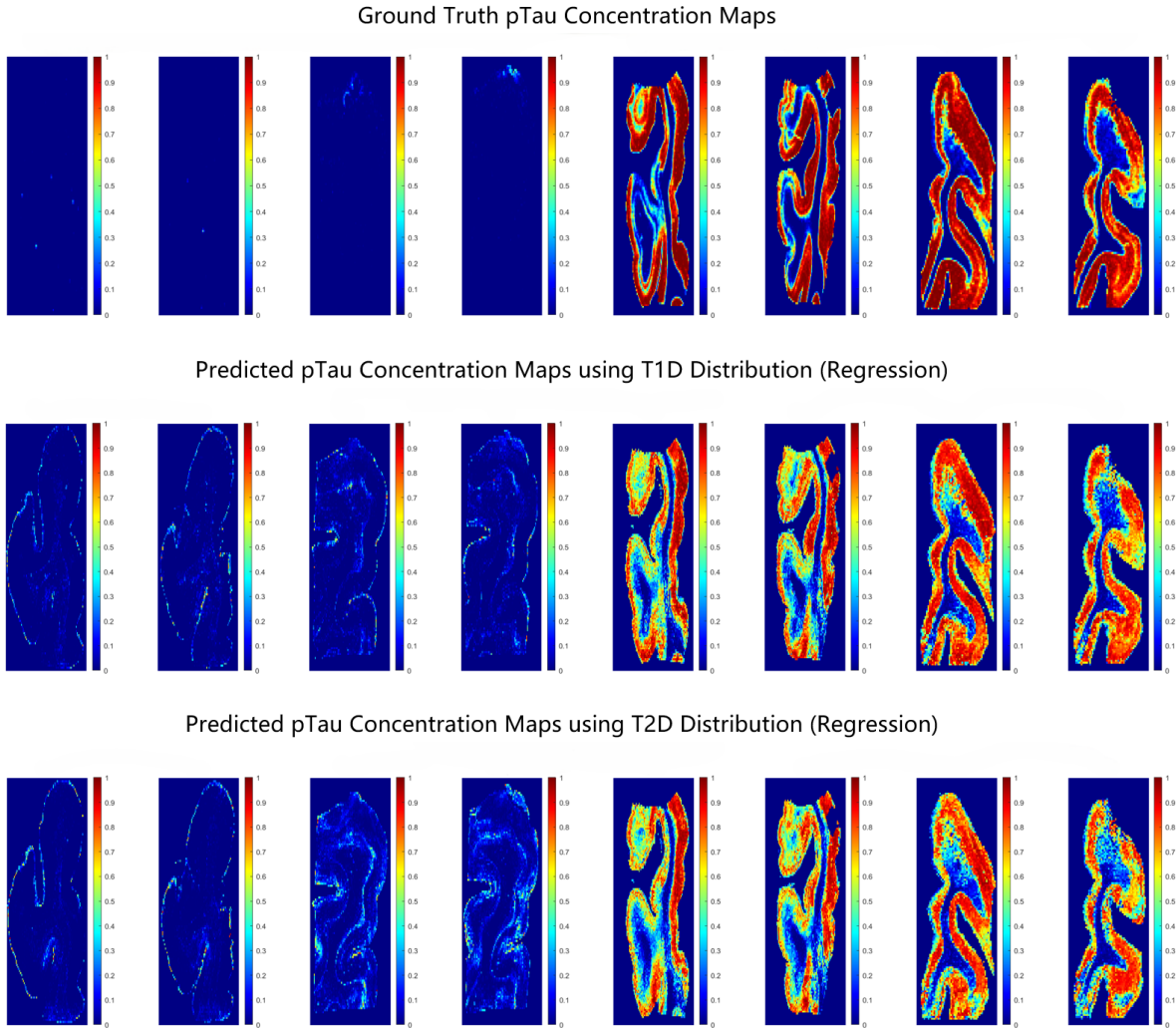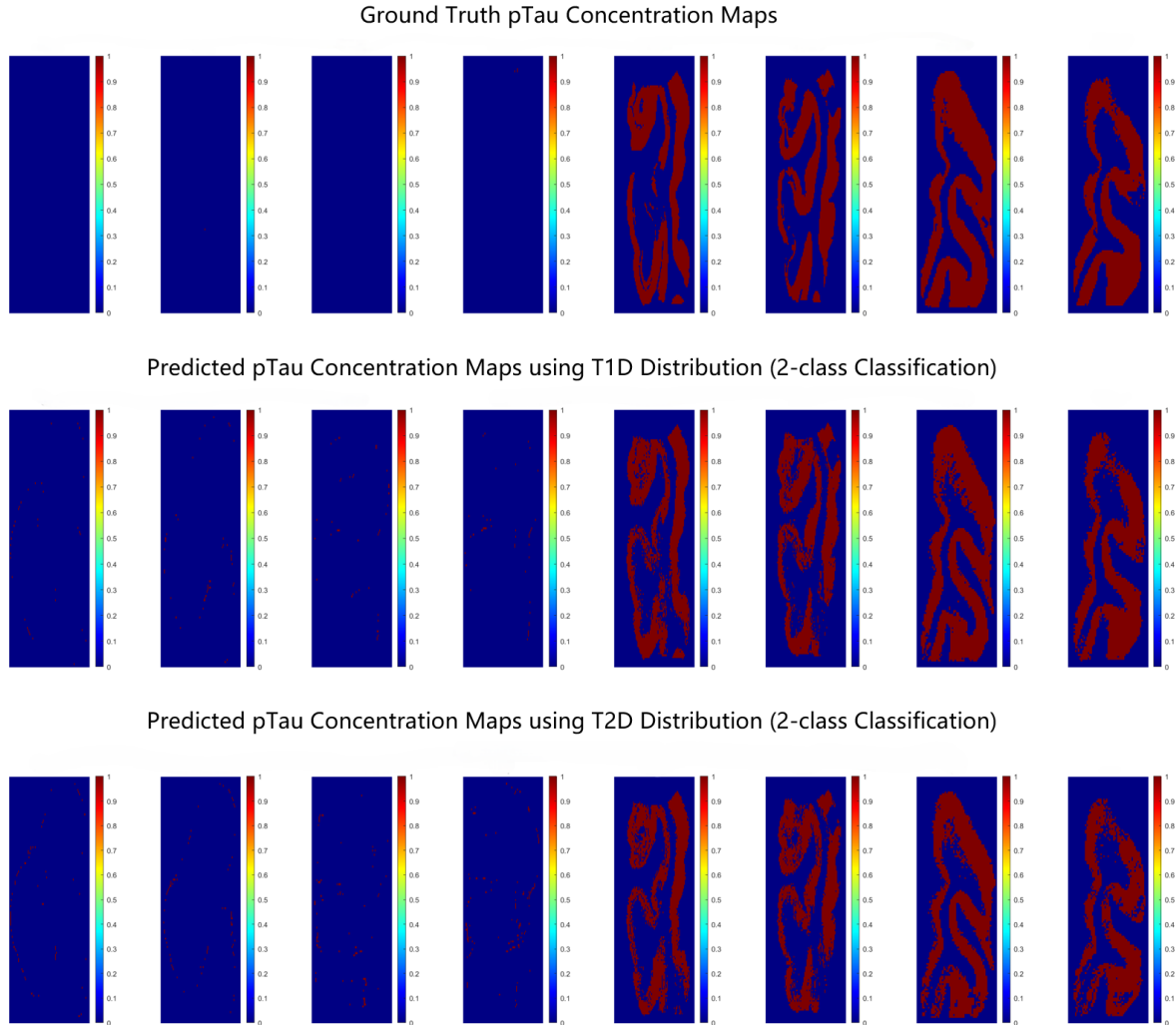
Figure 1: **Artifact-removed Ground Truth pTau Concentration Maps.** Top: Continuous pTau concentration map (regression target). Middle: 2-class pTau concentration map derived from the continuous concentration (2-class classification target). Bottom: 3-class pTau concentration map derived from the continuous concentration (3-class classification target). Left four slices correspond to Control subjects, and right four slices correspond to AD subjects.
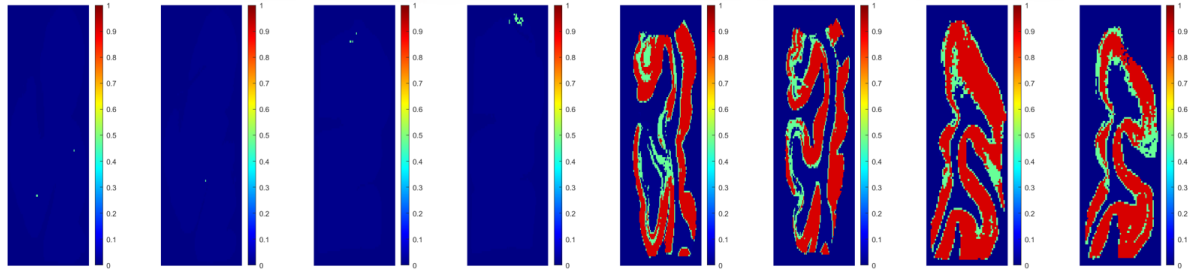
Figure 2: **Random Forest Regression Results Comparison.** Top: Ground truth continuous pTau concentration map. Middle: Predicted pTau concentration map using T1D joint distributions. Bottom: Predicted pTau concentration map using T2D joint distributions. All predictions were generated using cross-validation.

Ground Truth pTau Concentration Maps

Predicted pTau Concentration Maps using T1D Distribution (2-class Classification)

Predicted pTau Concentration Maps using T2D Distribution (2-class Classification)
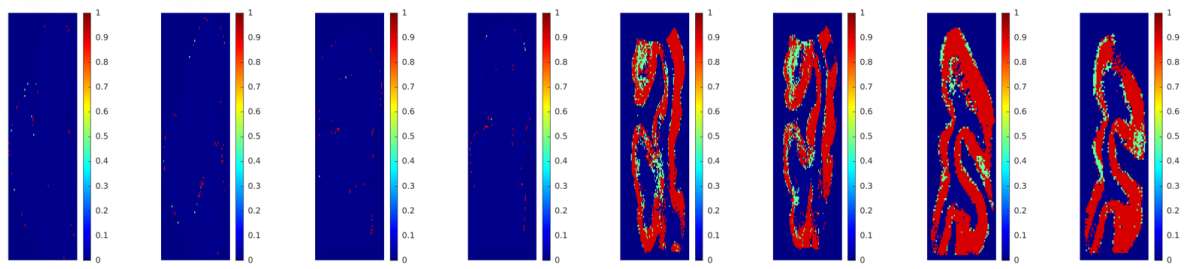
Figure 3: **Random Forest 2-class Classification Results Comparison.** Top: Ground truth 2-class pTau concentration map. Middle: Predicted pTau concentration map using T1D joint distributions. Bottom: Predicted pTau concentration map using T2D joint distributions. All predictions were generated using cross-validation.
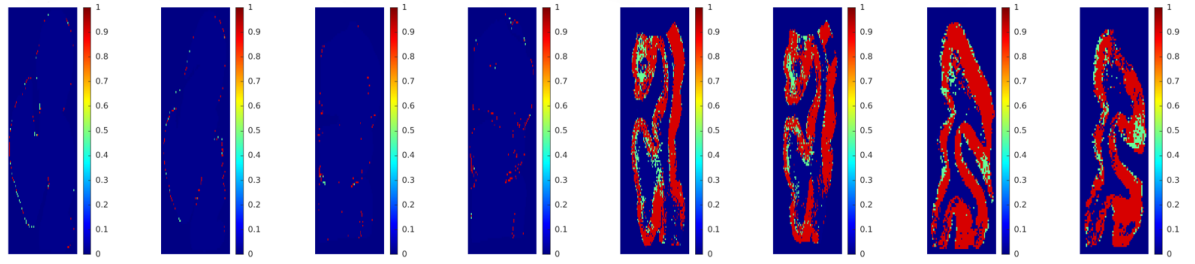
Figure 4: **Random Forest 3-class Classification Results Comparison.** Top: Ground truth 3-class pTau concentration map. Middle: Predicted pTau concentration map using T1D joint distributions. Bottom: Predicted pTau concentration map using T2D joint distributions. All predictions were generated using cross-validation.